

Deriving the Nonlinear Cosmological Power Spectrum and Bispectrum from Analytic Dark Matter Halo Profiles and Mass Functions

Chung-Pei Ma

*Department of Physics and Astronomy, University of Pennsylvania, Philadelphia PA 19104;
cpma@physics.upenn.edu*

and

J. N. Fry

Department of Physics, University of Florida, Gainesville FL 32611-8440; fry@phys.ufl.edu

ABSTRACT

We present an analytic model for the fully nonlinear power spectrum P and bispectrum Q of the cosmological mass density field. The model is based on physical properties of dark matter halos, with the three main model inputs being analytic halo density profiles, halo mass functions, and halo-halo spatial correlations, each of which has been well studied in the literature. We demonstrate that this new model can reproduce the power spectrum and bispectrum computed from cosmological simulations of both an $n = -2$ scale-free model and a low-density cold dark matter model. To enhance the dynamic range of these large simulations, we use the synthetic halo replacement technique of Ma & Fry (2000), where the original halos with numerically softened cores are replaced by synthetic halos of realistic density profiles. At high wavenumbers, our model predicts a slope for the nonlinear power spectrum different from the often-used fitting formulas in the literature based on the stable clustering assumption. Our model also predicts a three-point amplitude Q that is scale dependent, in contrast to the popular hierarchical clustering assumption. This model provides a rapid way to compute the mass power spectrum and bispectrum over all length scales where the input halo properties are valid. It also provides a physical interpretation of the clustering properties of matter in the universe.

Subject headings: cosmology : theory – dark matter – large-scale structure of universe

1. Introduction

Two conceptual pictures of galaxy clustering have been examined in the literature, the continuous hierarchical clustering model and the power-law cluster model (Peebles 1980, §61). In the hierarchical clustering model, which has emerged as the accepted model over the past two decades,

galaxy clustering is characterized by power-law correlation functions: the N -point correlation function ξ_N scales with configuration size as $\xi_N \propto r^{-\gamma_N} \propto \xi_2^{(N-1)}$, where $\gamma_N = (N - 1)\gamma$ and the two-point correlation function goes as $\xi_2 = \xi \propto r^{-\gamma}$. The hierarchical model is motivated by the observed power-law behavior $\gamma \approx 1.8$ of galaxy correlations (Groth & Peebles 1977; Fry & Peebles 1978), with a theoretical basis in a self-similar, scale-invariant solution to the equations of motion (Davis & Peebles 1977).

The alternative power-law cluster model has an even longer history (Neyman & Scott 1952; Peebles 1974, 1980; McClelland & Silk 1977; Scherrer & Bertschinger 1991; Sheth & Jain 1997; Valageas 1998; Yano & Gouda 1999). In this model, galaxies are placed in spherical clumps that are assumed to follow a power-law density profile $\rho(r) \propto r^{-\epsilon}$, with the centers of the clumps distributed randomly. The resulting two-point correlation function is also a power law with a logarithmic slope $\gamma = 2\epsilon - 3$. While it is possible to reproduce the observed two-point function by an appropriate choice of the power index $\epsilon = (3 + \gamma)/2 \approx 2.4$, Peebles and Groth (1975) pointed out that this model produces a three-point function that is too steep to be consistent with observations in the Zwicky and Lick catalogs.

In an earlier paper (Ma & Fry 2000a), we have shown that in the nonlinear regime, the three-point correlation function $\zeta = \xi_3$ of the cosmological mass density field does not exactly follow the prediction $\zeta \propto \xi^2$ of the hierarchical clustering model. These conclusions are drawn from study of high resolution numerical simulations of a cold dark matter (CDM) model with cosmological constant and of a model with scale-free initial conditions $P(k) \sim k^n$ with $n = -2$. In experiments replacing simulation dark matter halos with power-law density profiles, $\rho(r) \sim r^{-\epsilon}$, we have demonstrated that the behavior of the correlation functions in the nonlinear regime are determined by the halo profiles, but that it is not possible to match both the two- and three-point correlations with a single slope ϵ . These results differ from the predictions of both of these two conceptual models.

In this paper, we expand our previous study of the nonlinear two- and three-point correlation functions by investigating a new prescription that takes into account the non-power-law profiles of halos, the distribution of halo masses, and the spatial correlations of halo centers. Each of these ingredients has been well studied in the literature. We find that this halo model provides a good description of the two- and three-point correlation functions in both the $n = -2$ and CDM simulations over the entire range of scales from the weak clustering, perturbative regime on large length scales, to the strongly nonlinear regime on small length scales. Our result is approximately hierarchical over an intermediate range of scales, thus uniting the two pictures. An independent recent study by Seljak (2000), which appeared during completion of this work, has also examined the two-point power spectrum in a similar construction and has found that this type of approach can reproduce the power spectrum in the CDM model. The analytic model proposed here can be used to compute the two- and three-point correlation functions and their Fourier transforms, the power spectrum and bispectrum, over any range of scale where the input halo properties are valid.

In a subsequent paper (Ma & Fry 2000c), we study the predictions of this analytic halo model for the asymptotic nonlinear behavior of the N -point correlation functions and the pairwise velocities and examine the conditions required for stable clustering.

The outline of this paper is as follows. In §2 we describe the three input ingredients of the model: halo density profiles, halo mass functions, and halo-halo correlations. In §3 we assemble these ingredients and construct analytic expressions for the two-point correlation function $\xi(r)$ and the power spectrum $P(k)$. In §4 we do the same for the three-point correlation function $\zeta(r_1, r_2, r_3)$ and its Fourier transform, the bispectrum $B(k_1, k_2, k_3)$. In §5 we test the validity of this new model by comparing its predictions with results from numerical simulations of an $n = -2$ scale free model and a low-density CDM model with a cosmological constant (Λ CDM). We also present results of the synthetic halo replacement technique used to enhance the numerical resolution. In §6 we discuss further the physical meanings and implications of the model. In particular, we elaborate on two important implications of this model: deviations from the common assumptions of stable clustering and hierarchical clustering. Section 7 is a summary.

2. Model Ingredients

2.1. Halo Mass Density Profile

It has been suggested recently that the mass density profiles of cold dark matter halos have a roughly universal shape, generally independent of cosmological parameters (Navarro, Frenk, & White 1996, 1997)

$$\frac{\rho(r)}{\bar{\rho}} = \bar{\delta} u(r/R_s), \quad (1)$$

where $\bar{\delta}$ is a dimensionless density amplitude, R_s is a characteristic radius, and $\bar{\rho}$ is the mean background density. We consider two functional forms for the density profiles

$$\begin{aligned} u_I(x) &= \frac{1}{x^p(1+x)^{3-p}}, \\ u_{II}(x) &= \frac{1}{x^p(1+x^{3-p})}. \end{aligned} \quad (2)$$

Both forms have asymptotic behaviors x^{-p} at small x and x^{-3} at large x , but they differ in the transition region. The first form $u_I(x)$ with $p = 1$ is found to provide a good fit to simulation halos by Navarro et al. (1996, 1997), whereas the second form $u_{II}(x)$ with a steeper inner slope $p = 3/2$ is favored by Moore et al. (1998, 1999). Some independent simulations have produced halos that are well fit by the shallower $p = 1$ inner slope (e.g., Hernquist 1990; Dubinski & Carlberg 1991; Huss, Jain, & Steinmetz 1999), and others the steeper $p > 1$ slope (e.g., Fukushige and Makino 1997). Jing & Suto (2000) have recently reported a mass-dependent inner slope, with $p \approx 1.5$ for galactic-mass halos and $p \approx 1$ for cluster-mass halos. Many of these authors find that the outer profile scales as r^{-3} , but steeper outer profiles have also been suggested (Hernquist 1990; Dubinski

& Carlberg 1991). Given these uncertainties, we will consider in this paper both types of profiles in equation (2).

The parameters R_s and $\bar{\delta}$ in equation (1) are generally functions of the halo mass M . A concentration parameter,

$$c = \frac{R_{200}}{R_s}, \quad (3)$$

can be used to quantify the central density of a halo (Navarro et al. 1997), where R_{200} is the radius within which the average density is 200 times the mean density of the universe. Using $M = 800\pi \bar{\rho} R_{200}^3/3$, we can relate R_s and $\bar{\delta}$ to M and c , where the scale radius R_s is

$$R_s = \frac{1}{c} \left(\frac{3M}{800\pi\bar{\rho}} \right)^{1/3} = \frac{1.63 \times 10^{-5}}{\Omega_m^{1/3} c} \left(\frac{M}{h^{-1}M_\odot} \right)^{1/3} h^{-1}\text{Mpc}, \quad (4)$$

and the density amplitude $\bar{\delta}$ is

$$\begin{aligned} \bar{\delta}_I &= \frac{200 c^3}{3[\ln(1+c) - c/(1+c)]}, & p = 1, \\ \bar{\delta}_{II} &= \frac{100 c^3}{\ln(1+c^{3/2})}, & p = \frac{3}{2}. \end{aligned} \quad (5)$$

Typical values of c are in the range of a few to ten for type I and perhaps a factor of three smaller for type II. There is a weak dependence on mass, such that less massive halos have a larger central density (e.g., Cole & Lacey 1996; Tormen, Bouchet, & White 1997; Navarro et al. 1996, 1997; Jing & Suto 2000). This is understood in general terms as reflecting the mean density at the redshift z_f when the halo initially collapsed, $\bar{\delta} \sim (1+z_f)^3$. For $\Omega = 1$ this is $c \sim \sigma(M)$, or $c \propto M^{-(3+n)/6}$ in a scale-free model.

2.2. Halo Mass Function

The number density of halos with mass M within a logarithmic interval is often approximated by the prescription of Press & Schechter (1974),

$$\frac{dn}{d \ln M} = \sqrt{\frac{2}{\pi}} \frac{d \ln \sigma^{-1}}{d \ln M} \frac{\bar{\rho}}{M} \nu e^{-\nu^2/2}, \quad \nu = \frac{\delta_c}{\sigma(M)}, \quad (6)$$

where δ_c is a parameter characterizing the linear overdensity at the onset of gravitational collapse, and σ is the linear rms mass fluctuations in spheres of radius R

$$\sigma^2(M) = \int_0^\infty \frac{4\pi k^2 dk}{(2\pi)^3} P(k) W^2(kR), \quad (7)$$

where $W(x) = 3(\sin x - x \cos x)/x^3$ is the Fourier transform of a real-space tophat window function. The mass M is related to R by $M = 4\pi\bar{\rho}R^3/3$. For scale free models with a power law initial power

spectrum $P \propto k^n$, this is $\sigma = (M/M_*)^{-(3+n)/6}$. The parameter M_* characterizes the mass scale at the onset of nonlinearity, $\sigma(M_*) = 1$, and is related to the nonlinear wavenumber k_{nl} (defined as $\int_0^{k_{\text{nl}}} 4\pi k^2 dk P(k)/(2\pi)^3 = 1$) by

$$M_* = \frac{4\pi\bar{\rho}}{3} \frac{B(n)}{k_{\text{nl}}^3} = \frac{4\pi\bar{\rho}}{3} R_*^3, \quad (8)$$

where

$$\begin{aligned} B(n) &= (k_{\text{nl}}R_*)^3 = \left[(n+3) \int_0^\infty dx x^{n+2} W^2(x) \right]^{3/(n+3)}, \\ B^{(3+n)/3} &= \sin \left[(n+2) \frac{\pi}{2} \right] \Gamma(n+2) \frac{9(2^{-n})(3+n)}{(-n)(1-n)(3-n)} \end{aligned} \quad (9)$$

(defined for $-3 \leq n < 1$). Various modifications to the Press-Schechter mass function have been suggested (e.g., Sheth & Tormen 1999; Lee & Shandarin 1999; Jenkins et al. 2000) to improve the accuracy of the original formula.

2.3. Halo-Halo Correlations

Dark matter halos do not cluster in the same way as the mass density field. On large scales, a bias parameter b is typically used to quantify this difference. Let $\xi_{\text{halo}}(r; M, M')$ be the two-point correlation function of halos with masses M and M' , $\xi_{\text{lin}}(r)$ be the linear correlation function for the mass density field, and P_{halo} and P_{lin} be the corresponding power spectra. On large length scales, we assume a linear bias and write

$$\begin{aligned} \xi_{\text{halo}}(r; M, M') &= b(M) b(M') \xi_{\text{lin}}(r), \\ P_{\text{halo}}(k; M, M') &= b(M) b(M') P_{\text{lin}}(k). \end{aligned} \quad (10)$$

Based on the peak and the Press-Schechter formalism, Mo & White (1996) developed a model for the linear bias $b(M)$, which is later modified by Jing (1998) to be

$$b(M) = \left(1 + \frac{\nu^2 - 1}{\delta_c} \right) \left(\frac{1}{2\nu^4} + 1 \right)^{0.06 - 0.02n}, \quad \nu = \frac{\delta_c}{\sigma(M)}. \quad (11)$$

The original formula for $b(M)$ by Mo & White includes only the first factor above; the second factor, dependent on the primordial spectral index n , is obtained empirically for an improved fit to simulation results at the lower mass end (Jing 1998). In this bias model, $b(M)$ is below unity for $M \lesssim M_*$ (where $\sigma(M_*) = 1$) and reaches ~ 0.5 for $M \lesssim 0.01M_*$. Small dark matter halos are therefore anti-biased relative to the mass density. For $M \gtrsim M_*$, $b(M)$ increases monotonically with the halo mass and reaches $b \sim 10$ at $M \sim 100 M_*$. Nonlinear effects on the bias have been studied (Kravtsov & Klypin 1999 and references therein), but they are unimportant in our model because the halo-halo correlation terms contribute significantly only on large length scales in the linear regime (see §3 and 4).

Similarly, we use higher order bias parameters to relate the higher-order correlation functions for halos and mass density. In this paper we examine the three-point correlation function $\zeta(r_1, r_2, r_3)$ and its Fourier transform, the bispectrum $B(k_1, k_2, k_3)$ (see §4 for a more detailed discussion). On large length scales where the amplitude of δ is small, perturbation theory can be used to relate the lowest order contribution to the bispectrum of the mass density to the linear power spectrum P_{lin} (Fry 1984):

$$\begin{aligned} B^{(0)}(k_1, k_2, k_3) &= F_{12} P_{\text{lin}}(k_1) P_{\text{lin}}(k_2) + F_{23} P_{\text{lin}}(k_2) P_{\text{lin}}(k_3) + F_{31} P_{\text{lin}}(k_3) P_{\text{lin}}(k_1), \\ F_{ij} &= \frac{10}{7} + (k_i/k_j + k_j/k_i) (\hat{\mathbf{k}}_i \cdot \hat{\mathbf{k}}_j) + \frac{4}{7} (\hat{\mathbf{k}}_i \cdot \hat{\mathbf{k}}_j)^2. \end{aligned} \quad (12)$$

Using this perturbative result and the results of Mo, Jing, & White (1997), we can write the halo bispectrum as

$$\begin{aligned} B_{\text{halo}}(k_1, k_2, k_3; M, M', M'') &= [b(M)b(M')b(M'') F_{12} + b(M)b(M')b_2(M'')] P_{\text{lin}}(k_1) P_{\text{lin}}(k_2) \\ &+ [b(M)b(M')b(M'') F_{23} + b(M)b_2(M')b(M'')] P_{\text{lin}}(k_2) P_{\text{lin}}(k_3) \\ &+ [b(M)b(M')b(M'') F_{31} + b_2(M)b(M')b(M'')] P_{\text{lin}}(k_3) P_{\text{lin}}(k_1), \end{aligned} \quad (13)$$

where $b(M)$ is given by equation (11), and the quadratic bias parameter $b_2(M)$ is

$$b_2(M) = \frac{8}{21} \frac{(\nu^2 - 1)}{\delta_c} + \left(\frac{\nu}{\delta_c} \right)^2 (\nu^2 - 3). \quad (14)$$

For the special equilateral case of $k_1 = k_2 = k_3 = k$, equation (13) simplifies to

$$\begin{aligned} B_{\text{halo}}^{\text{eq}}(k; M, M', M'') &= \left[\frac{12}{7} b(M)b(M')b(M'') + b(M)b(M')b_2(M'') \right. \\ &\left. + b(M)b_2(M')b(M'') + b_2(M)b(M')b(M'') \right] P_{\text{lin}}^2(k). \end{aligned} \quad (15)$$

In practice, the terms involving $b_2(M)$ in equations (13) and (15) make only a small net contribution. For simplicity, we will therefore not include this term in the subsequent derivations and calculations.

3. Two-Point Statistics: $\xi(r)$ and $P(k)$

We now construct our analytic halo model for the two-point correlation function $\xi(r)$ and the power spectrum $P(k)$. The two-point correlation function of the cosmological mass density field $\delta = \delta\rho/\bar{\rho}$ is

$$\xi(\mathbf{r}) = \langle \delta(\mathbf{x}) \delta(\mathbf{x} + \mathbf{r}) \rangle. \quad (16)$$

The Fourier transform of $\xi(r)$ is the mass power spectrum $P(k) = \int d^3r e^{-i\mathbf{k}\cdot\mathbf{r}} \xi(r)$, which is related to the density field in k -space by $\langle \delta(\mathbf{k}_1) \delta(\mathbf{k}_2) \rangle = P(k_1) (2\pi)^3 \delta_D(\mathbf{k}_1 + \mathbf{k}_2)$, where δ_D is the Dirac delta-function.

The two-point correlation function measures the excess probability above the Poisson distribution of finding a pair of objects with separation r (Peebles 1980). The objects can be taken to be dark matter particles, most of which cluster gravitationally in the form of dark matter halos. One should therefore be able to express ξ for the density field in terms of properties of dark matter halos. In this picture, we can write the contributions to ξ as two separate terms, one from particle pairs in the same halo, and the other from pairs that reside in two different halos. In realistic cosmological models, dark matter halos exhibit a spectrum of masses that can be characterized by a distribution function dn/dM , and the halo centers are spatially correlated. Taking these factors into consideration, we can write the two-point correlation function for δ in terms of the halo density profile $u(x)$, halo mass function dn/dM , and halo-halo correlation function ξ_{halo} discussed in §2. We write

$$\xi(r) = \xi_{1h}(r) + \xi_{2h}(r), \quad (17)$$

where the subscripts “1h” and “2h” denote contributions from particle pairs in “1-halo” and “2-halos”, respectively, and

$$\begin{aligned} \xi_{1h}(r) &= \int d^3 r' \int dM \frac{dn}{dM} \bar{\delta}^2 u(r'/R_s) u(|\mathbf{r}' + \mathbf{r}|/R_s) \\ \xi_{2h}(r) &= \int d^3 r' d^3 r'' \int dM' \frac{dn}{dM'} \bar{\delta}' u(r'/R'_s) \int dM'' \frac{dn}{dM''} \bar{\delta}'' u(r''/R''_s) \xi_{\text{halo}}(|\mathbf{r}' - \mathbf{r}'' + \mathbf{r}|) \\ &= \int d^3 r' d^3 r'' \left[\int dM \frac{dn}{dM} \bar{\delta} u(r'/R_s) b(M) \right] \left[\int dM \frac{dn}{dM} \bar{\delta} u(r''/R_s) b(M) \right] \\ &\quad \times \xi_{\text{lin}}(|\mathbf{r}' - \mathbf{r}'' + \mathbf{r}|). \end{aligned} \quad (18)$$

These expressions arise from averaging over displacements \mathbf{r}' , \mathbf{r}'' of halo centers from the particle positions \mathbf{r}_1 , \mathbf{r}_2 , where $r = |\mathbf{r}_1 - \mathbf{r}_2|$. In the last expression above, we have used the bias model of equation (10) to relate the halo-halo correlation function ξ_{halo} to the linear correlation function ξ_{lin} of the mass density field.

As we will show in §5, the dominant contribution to the two-point correlation function in the nonlinear regime on small length scales is from the first, 1-halo term ξ_{1h} for particle pairs that reside in the same halos. This makes intuitive sense, because closely spaced particle pairs are most likely to be found in the same halo. This term is determined by the convolution of the dimensionless density profile with itself,

$$\lambda(x) = \int d^3 y u(y) u(|\mathbf{x} + \mathbf{y}|). \quad (19)$$

For many forms of $u(x)$, the angular integration in this equation is analytic, and λ can be reduced to a simple one-dimensional integral over y . For some special cases, λ can even be reduced to an analytic expression. We leave the detailed results for λ to the Appendix.

In k -space, the convolutions in equation (18) for $\xi(r)$ become simple products. Using $\tilde{u}(q)$ to denote the Fourier transform of $u(x)$, where $\tilde{u}(q) = \int d^3 x u(x) e^{-iq \cdot x}$, we can readily transform equation (18) into expressions for the mass power spectrum:

$$P(k) = P_{1h}(k) + P_{2h}(k), \quad (20)$$

where the 1-halo and 2-halo terms are

$$\begin{aligned}
 P_{1h}(k) &= \int dM \frac{dn}{dM} [R_s^3 \bar{\delta} \tilde{u}(kR_s)]^2 \\
 P_{2h}(k) &= \int dM \frac{dn}{dM} R_s^3 \bar{\delta} \tilde{u}(kR_s) \int dM' \frac{dn}{dM'} R_s'^3 \bar{\delta}' \tilde{u}(kR_s') P_{\text{halo}}(k) \\
 &= \left[\int dM \frac{dn}{dM} R_s^3 \bar{\delta} \tilde{u}(kR_s) b(M) \right]^2 P_{\text{lin}}(k).
 \end{aligned} \tag{21}$$

To arrive at the last expression above, we have again used the bias model of equation (10). For computational efficiency, we find that the algebraic expressions

$$\begin{aligned}
 \tilde{u}_I(q) &= \frac{4\pi \{ \ln(e + 1/q) - \ln[\ln(e + 1/q)]/3 \}}{(1 + q^{1.1})^{2/1.1}}, & p = 1 \\
 \tilde{u}_{II}(q) &= \frac{4\pi \{ \ln(e + 1/q) + 0.25 \ln[\ln(e + 1/q)] \}}{1 + 0.8 q^{1.5}}, & p = \frac{3}{2}
 \end{aligned} \tag{22}$$

provide excellent fits for the profiles of Navarro et al. (1997) and Moore et al. (1999), with less than 4% rms error for form I and less than 1% rms error for form II. The functional form is chosen to reproduce the asymptotic behaviors: $\tilde{u} \sim 4\pi \ln q$ at small q (with no radial cutoff), and $\tilde{u} \propto q^{-2}$ (type I) and $\tilde{u} \propto q^{-3/2}$ (type II) at large q .

The two-point $\xi(r)$ and $P(k)$ can now be computed analytically from equations (18) and (21). The inputs are equation (2) or (22) for the halo density profile $u(x)$ or $\tilde{u}(q)$, equations (4) and (5) for R_s and $\bar{\delta}$, equation (6) for the halo mass function dn/dM , and equation (10) for the halo-halo correlation function. Since the halo density profile appears to have a nearly universal form regardless of background cosmology, $\xi(r)$ and $P(k)$ depend on cosmological parameters mainly through $\sigma(M)$ of equation (7) and the halo concentration $c(M)$ or central density $\bar{\delta}(M)$. (See Ma & Fry 2000c for a more detailed discussion of $c(M)$.)

4. Three-Point Statistics: ζ and B

Here we construct our analytic halo model for the three-point correlation function ζ and the bispectrum B . The joint probability of finding three objects in volume elements dV_1, dV_2 , and dV_3 is given by

$$dP = [1 + \xi(r_1) + \xi(r_2) + \xi(r_3) + \zeta(r_1, r_2, r_3)] \bar{n}^3 dV_1 dV_2 dV_3, \tag{23}$$

where $\xi(r)$ and $\zeta(r_1, r_2, r_3)$ are the two- and three-point correlation functions, respectively, \bar{n} is the mean number density of objects, and r_1, r_2 and r_3 are the lengths of the sides of the triangle defined by the three objects (Peebles 1980). The Fourier transform of the three-point correlation function $\zeta(r_1, r_2, r_3)$ is the bispectrum $B(k_1, k_2, k_3)$, which is related to the density field in k -space by $\langle \delta(\mathbf{k}_1) \delta(\mathbf{k}_2) \delta(\mathbf{k}_3) \rangle = B(k_1, k_2, k_3) (2\pi)^3 \delta_D(\mathbf{k}_1 + \mathbf{k}_2 + \mathbf{k}_3)$. The bispectrum depends on any three parameters that define a triangle in k -space. A particular simple configuration to study is the

equilateral triangle ($k_1 = k_2 = k_3 = k$), and in this case the bispectrum B^{eq} depends only on a single wavenumber.

Similar to the two-point halo model of §3, we can write the contributions to the three-point correlation function ζ of the mass density as three separate terms, each term representing particle triplets that reside in a single halo, two distinct halos, or three distinct halos. Taking into account the halo mass distribution and halo-halo correlations discussed in §2, we obtain

$$\zeta(r_1, r_2, r_3) = \zeta_{1h}(r_1, r_2, r_3) + \zeta_{2h}(r_1, r_2, r_3) + \zeta_{3h}(r_1, r_2, r_3), \quad (24)$$

where the separate 1-halo, 2-halo, and 3-halo terms are

$$\begin{aligned} \zeta_{1h}(r_1, r_2, r_3) &= \int d^3r \int dM \frac{dn}{dM} \bar{\delta}^3 u(r/R_s) u(|\mathbf{r} + \mathbf{r}_1 - \mathbf{r}_2|/R_s) u(|\mathbf{r} + \mathbf{r}_1 - \mathbf{r}_3|/R_s) \\ \zeta_{2h}(r_1, r_2, r_3) &= \int d^3r d^3r' \int dM \frac{dn}{dM} \bar{\delta}^2 u(r/R_s) u(|\mathbf{r} + \mathbf{r}_1 - \mathbf{r}_2|/R_s) \int dM' \frac{dn}{dM'} \bar{\delta}' u(r'/R'_s) \\ &\quad \times \xi_{\text{halo}}(|\mathbf{r} - \mathbf{r}' + \mathbf{r}_1 - \mathbf{r}_3|) + \text{sym.}(1,2,3) \\ \zeta_{3h}(r_1, r_2, r_3) &= \int d^3r d^3r' d^3r'' \int dM \frac{dn}{dM} \bar{\delta} u(r/R_s) \int dM' \frac{dn}{dM'} \bar{\delta}' u(r'/R'_s) \\ &\quad \times \int dM'' \frac{dn}{dM''} \bar{\delta}'' u(r''/R''_s) \zeta_{\text{halo}}(\mathbf{r} + \mathbf{r}_1, \mathbf{r}' + \mathbf{r}_2, \mathbf{r}'' + \mathbf{r}_3). \end{aligned} \quad (25)$$

The dominant contribution to the three-point correlation function in the nonlinear regime is from the first term ζ_{1h} , which comes from particle triplets that reside in the same halo. This term is determined by the convolution $\gamma(\mathbf{x}_1, \mathbf{x}_2) = \int d^3y u(y) u(|\mathbf{y} + \mathbf{x}_1|) u(|\mathbf{y} + \mathbf{x}_2|)$ of three factors of the density profile $u(x)$, and is analogous to the convolution λ in equation (19) for the one-halo term ζ_{1h} in the two-point correlation function.

The bispectrum of the mass density field δ in k -space can be obtained by Fourier transforming the equations above. We find

$$B(k_1, k_2, k_3) = B_{1h}(k_1, k_2, k_3) + B_{2h}(k_1, k_2, k_3) + B_{3h}(k_1, k_2, k_3), \quad (26)$$

where

$$\begin{aligned} B_{1h}(k_1, k_2, k_3) &= \int dM \frac{dn}{dM} [R_s^3 \bar{\delta} \tilde{u}(k_1 R_s)] [R_s^3 \bar{\delta} \tilde{u}(k_2 R_s)] [R_s^3 \bar{\delta} \tilde{u}(k_3 R_s)] \\ B_{2h}(k_1, k_2, k_3) &= \int dM \frac{dn}{dM} [R_s^3 \bar{\delta} \tilde{u}(k_1 R_s)] [R_s^3 \bar{\delta} \tilde{u}(k_2 R_s)] \\ &\quad \times \int dM' \frac{dn}{dM'} R_s'^3 \bar{\delta}' \tilde{u}(k_3 R'_s) P_{\text{halo}}(k_3; M, M') + \text{sym.}(1,2,3) \\ B_{3h}(k_1, k_2, k_3) &= \int dM \frac{dn}{dM} R_s^3 \bar{\delta} \tilde{u}(k_1 R_s) \int dM' \frac{dn}{dM'} R_s'^3 \bar{\delta}' \tilde{u}(k_2 R'_s) \\ &\quad \times \int dM'' \frac{dn}{dM''} R_s''^3 \bar{\delta}'' \tilde{u}(k_3 R''_s) B_{\text{halo}}(k_1, k_2, k_3; M, M', M''). \end{aligned} \quad (27)$$

The halo-halo power spectrum $P_{\text{halo}}(k)$ and bispectrum $B_{\text{halo}}(k_1, k_2, k_3)$ are related to the linear mass power spectrum $P_{\text{lin}}(k)$ by equations (10) and (13).

The expressions for the mass bispectrum above simplify considerably for the equilateral triangle configuration, and

$$B^{\text{eq}}(k) = B_{1h}^{\text{eq}}(k) + B_{2h}^{\text{eq}}(k) + B_{3h}^{\text{eq}}(k), \quad (28)$$

where

$$\begin{aligned} B_{1h}^{\text{eq}}(k) &= \int dM \frac{dn}{dM} [R_s^3 \bar{\delta} \tilde{u}(kR_s)]^3 \\ B_{2h}^{\text{eq}}(k) &= 3 \left[\int dM \frac{dn}{dM} [R_s^3 \bar{\delta} \tilde{u}(kR_s)]^2 b(M) \right] \left[\int dM \frac{dn}{dM} R_s^3 \bar{\delta} \tilde{u}(kR_s) b(M) \right] P_{\text{lin}}(k) \\ B_{3h}^{\text{eq}}(k) &= \left[\int dM \frac{dn}{dM} R_s^3 \bar{\delta} \tilde{u}(kR_s) b(M) \right]^3 \frac{12}{7} P_{\text{lin}}^2(k). \end{aligned} \quad (29)$$

Here we have written out explicitly the bias factors $b(M)$ using equations (10) and (15), and we have neglected terms with $b_2(M)$ as discussed in §2.3.

5. N -body Experiments and Numerical Results

In this section we compare the predictions of our analytical model described in §2, 3, and 4 with results from cosmological N -body simulations. We examine two cosmological models: an $n = -2$ scale-free model and a low-density Λ CDM model. These are the same simulations studied in Ma & Fry (2000a). The $n = -2$ simulation has 256^3 particles and a Plummer force softening length of $L/5120$, where L is the box length. The Λ CDM model is spatially flat with matter density $\Omega_m = 0.3$ and cosmological constant $\Omega_\Lambda = 0.7$. This run has 128^3 particles and is performed in a $(100 \text{ Mpc})^3$ comoving box with a comoving force softening length of 50 kpc for Hubble parameter $h = 0.75$. The baryon fraction is set to zero for simplicity. The primordial power spectrum has a spectral index of $n = 1$, and the density fluctuations are drawn from a random Gaussian distribution. The gravitational forces are computed with a particle-particle particle-mesh (P^3M) code (Ferrell & Bertschinger 1994). We compute the density field δ on a grid from particle positions using the second-order triangular-shaped cloud (TSC) interpolation scheme. A fast Fourier transform is then used to obtain δ in k -space. The k -space TSC window function is deconvolved to correct for smearing in real space due to the interpolation, and shot noise terms are subtracted to correct for discreteness effects. We then compute the second and third moments of the density amplitudes in Fourier space.

We show results for the power spectrum as the dimensionless variance $\Delta(k) \equiv 4\pi k^3 P(k)/(2\pi)^3$. A useful dimensionless three-point statistic is the hierarchical three-point amplitude

$$Q(k_1, k_2, k_3) \equiv \frac{B(k_1, k_2, k_3)}{P(k_1)P(k_2) + P(k_2)P(k_3) + P(k_3)P(k_1)}. \quad (30)$$

The three-point amplitude Q has the convenient feature that for the lowest nonvanishing result in perturbation theory, Q is independent of time and the overall amplitude of P ; for scale-free models with a power-law P , Q is independent of overall scale as well. To lowest order, it follows from equation (12) that the equilateral bispectrum has a particularly simple form, $B^{(0)}(k) = \frac{12}{7} P_{\text{lin}}^2(k)$, and we have $Q^{(0)}(k) = \frac{4}{7}$, independent of the power spectrum.

5.1. Synthetic Halo Replacement

To investigate the numerical effects of limited resolution in the simulations, we have experimented with the distribution of matter in halos identified in the simulations. In these experiments, we keep the locations and masses of the halos unchanged but redistribute the subset of particles which lies within the virial radius R_{200} (the radius within which the mean overdensity is 200) of each halo according to a prescribed density profile. We then recompute the two- and three-point statistics Δ and Q from the redistributed particle positions as well as the original non-halo particles, which remain at their original positions. By using density profiles obtained empirically from higher-resolution simulations of individual halos, this recipe allows us to model accurately the inner regions of the halos on scales below the numerical softening length scale while at the same time preserving all the large-scale information available in the large parent simulation. This technique should also be useful for other studies that are sensitive to the inner halo density profiles, for example the ray-tracing method in gravitational lensing.

Ma & Fry (2000a) have used this replacement technique to experiment with synthetic halos that follow a pure power-law profile $u \propto r^{-\epsilon}$. It is found that $\Delta(k)$ and $Q(k)$ at high- k indeed obey $\Delta(k) \propto k^{2\epsilon-3}$ and $Q(k) \propto k^{3-\epsilon}$ as predicted by the simple power-law model of Peebles (1974). The scaling works even in the presence of the full distribution of matter outside the halo cores. Here we extend this replacement technique to more realistic halo profiles of equation (2). Figures 1 and 2 illustrate the effects on the matter power spectrum and bispectrum when the original halos in large cosmological simulations are replaced by synthetic halos with the density profile $u_{II} = 1/(x^{3/2} + x^3)$ of equation (2). For the $n = -2$ scale-free model, the concentration parameter is taken to be $c(M) = 3(M_*/M)^{1/6}$, which is consistent with Navarro et al. (1997) and has the expected scaling with mass, $c \propto M^{-(3+n)/6}$, in a scale-free model. For Λ CDM models, we use $c(M) = 5(M_*/M)^{1/6}$ as suggested by Figure 3 of Moore et al. (1999). We note, however, that $c(M)$ from various recent simulations has shown a large scatter, and its functional form depends on the exact form of the density profile used. For the Λ CDM model and form $u_{II} = 1/(x^{3/2} + x^3)$, for example, a flatter and smaller $c(M) = 3(M_*/M)^{0.084}$ appears to be preferred by Jing & Suto (2000) and Navarro et al. (1997). The results of Tormen et al. (1997) and Cole & Lacey (1996) are also only marginally consistent with each other. A more detailed investigation of the different forms of $c(M)$ can be found in Ma & Fry (2000c).

In Figures 1 and 2, the agreement at low values of k between the original and synthetic halos is excellent, confirming that the correlation functions on larger length scales are insensitive to

the spatial distribution of particles in the halo cores. The only significant difference between the simulation and synthetic halos appears at small length scales, where the coarser resolution of the simulation blurs out the structure of the inner halo and results in an inner profile flatter than in equation (2). This effect is manifested in the bending over of the dashed curves for $P(k)$ in Figures 1 and 2 at high k , and is corrected for when the synthetic halos are used.

5.2. N -body Results vs. Analytic Halo Model

We now proceed to compare the predictions of the analytic model of §2 – §4 with the numerical results from cosmological simulations. Figures 3 and 4 show the k -space density variance $\Delta(k)$ (upper panel) and the three-point amplitude $Q_{\text{eq}}(k)$ for equilateral triangles for the $n = -2$ scale-free model and the Λ CDM model. The solid black curves are the model predictions computed from equations (21) and (29). The contribution from the single-halo and multiple-halo terms are shown separately as dashed curves. For the density profile, we use the same $u_{II} = 1/(x^{3/2} + x^3)$ and concentration parameters as in Figures 1 and 2. For the mass function, we use the Press-Schechter formula but reduce its overall amplitude by 25%, which we find necessary in order to match the halo mass functions for our numerical simulations. This overestimation of halo numbers with $M \sim M_*$ by Press-Schechter is a well known result reported in many other studies (see Jenkins et al. 2000 and references therein). The mass limits for the integrals in equations (21) and (29) do not significantly affect the model predictions for the total Δ or Q . Raising the lower mass limit does reduce the contribution from lower mass halos and hence lower the high- k amplitudes of the multiple halo terms Δ_{2h} , Q_{2h} , and Q_{3h} , but these terms make negligible contributions to the total Δ and Q .

As discussed in §3 and 4, the nonlinear parts of both the two- and three-point statistics are determined by the dominant 1-halo term because the closely spaced particle pairs and triplets mostly reside in the same halos. The multiple-halo terms are therefore significant only on larger length scales comparable to the separation between halos. Their inclusion, however, is necessary for the transition into the linear regime.

For the $n = -2$ model in Figure 3, we plot the results against the scaled k/k_{nl} , where k_{nl} characterizes the length scale that is becoming nonlinear and is defined by $\int_0^{k_{\text{nl}}} d^3k P_{\text{lin}}(a, k)/(2\pi)^3 = 1$. Three time outputs are shown, where the expansion factor (1 initially) and k_{nl} (in units of $2\pi/L$) are: $(a, k_{\text{nl}}) = (13.45, 29)$, $(19.03, 14.5)$, and $(26.91, 7.25)$ (from left to right). For the two-point $\Delta(k)$, the agreement between the model prediction and the simulations is excellent. The three simulation outputs also overlap well, indicating that self-similarity is obeyed, as reported in Jain & Bertschinger (1998). For the three-point Q_{eq} , however, self-similar scaling does not hold as rigorously (Ma & Fry 2000a). It is interesting to note that the analytic prediction agrees most closely with the earliest output $(a, k_{\text{nl}}) = (13.45, 29)$ (green curve). This provides further evidence to the suggestion of Ma & Fry (2000a) that the later outputs of the $n = -2$ simulation may be affected by the finite volume of the simulation box. For the Λ CDM model in Figure 4, the

analytic model again provides a good match to the N -body results within the fluctuations among the simulations. We illustrate the numerical effects due to box sizes by showing results from two runs with volume $(100 \text{ Mpc})^3$ and $(640 \text{ Mpc})^3$. The model predictions extend well beyond the resolution of the simulations.

The real-space two-point correlation function for the $n = -2$ and Λ CDM models is shown in Figures 5 and 6. For the halo model predictions, we have chosen to show only the results for the 1-halo term ξ_{1h} because this term dominates the interesting nonlinear portion of ξ . The agreement between the halo model (dashed curves) and the simulations (symbols) is again excellent. For the 2-halo terms ξ_{2h} , the computation can be done more easily in k -space as shown in Figures 3 and 4, so we do not include them here.

For comparison, we plot in Figures 3–6 the results from the commonly used fitting formulas for the nonlinear power spectrum (Hamilton et al. 1991; Jain et al. 1995; Peacock & Dodds 1996; Ma 1998; Ma et al. 1999). While the formulas provide a good approximation to $\Delta(k)$ up to $k/k_{\text{nl}} \sim 50$ for the $n = -2$ model and $k \sim 20 h \text{ Mpc}^{-1}$ for the Λ CDM model, the figures show that significant deviations occur at higher k , and the fitting formula and our current model predict different high- k slopes for $\Delta(k)$. Since the high- k behavior of the fitting formulas has been constructed to obey the stable clustering prediction, this discrepancy has an important implication for the validity of stable clustering, which we discuss briefly in the next section and at length in Ma & Fry (2000c).

6. Discussion

We have constructed a physical model for the correlation functions of the mass density field in which the correlations are derived from properties of dark matter halos. We have described in detail the input, construction, and results of this model in §2 – §5. We now examine more closely its physical meanings and implications in three separate regimes.

On scales larger than the size of the largest halo, the contributions from separate halos dominate, and (by design) the model reproduces the results of perturbation theory. On intermediate scales, $1/R_* \lesssim k \lesssim 1/R_s(M_*)$, because of the exponential cutoff in the mass function dn/dM at the high mass end, the contribution to the volume integrals in equation (18) is dominated by the large- r regime where the halo profiles are roughly r^{-3} . The correlation functions therefore behave approximately as predicted by the power-law model with $\epsilon = 3$, i.e., $\Delta \propto k^{2\epsilon-3} \sim k^3$ and $Q \propto k^{3-\epsilon} \sim \text{constant}$. This is why Q exhibits an approximately flat plateau at intermediate k in the bottom panels of Figures 3 and 4.

On the smallest and most nonlinear scales, the correlation functions probe the innermost regions of the halos. Intriguingly, the halo model predicts on these scales a behavior that is different from either the frequently-assumed stable clustering result of $\Delta(k) \propto k^\gamma$ with $\gamma = (9 + 3n)/(5 + n)$ (Davis & Peebles 1977), or the power-law profile result of $\gamma = 2\epsilon - 3$. The implication of departure from stable clustering is significant because all the fitting formulas for the nonlinear $P(k)$ in the

literature (see §5.2) have been constructed to approach the stable clustering limit at high k . A more detailed study on the criteria for stable clustering in this model is given in a separate paper (Ma & Fry 2000c).

The origin of the deviation from stable clustering in the model at high- k can be understood as follows. For the two-point function, as k becomes large, the one-halo integral $P_{1h}(k)$ in equation (21) converges before the exponential cutoff, and is dominated by contributions near the mass scale for which $kR_s = 1$. The behavior now depends on the mass distribution function. The various mass functions discussed in §2.2 have the same general behavior of $dn/dM \propto M^{-2} \nu^\alpha e^{-\nu^2/2}$, where $\nu = \delta_c/\sigma$. The Press-Schechter form assumes $\alpha = 1$ (see eq. [6]), while others (e.g., Sheth & Tormen 1999; Jenkins et al. 2000) suggest a flatter slope of $\alpha \approx 0.4$ for the lower mass halos. Since the scale radius R_s depends on mass as $R_s = R_{200}/c \propto M^{1/3}/M^{-(3+n)/6} \propto M^{(5+n)/6}$, and $R_s^3 \bar{\delta} \propto M$ (up to logarithmic factors), we find from equation (21) that the power spectrum at high k goes as

$$\Delta(k) \approx \Delta_{1h}(k) \propto k^3 \int dM \nu^\alpha \tilde{u}^2(kR_s). \quad (31)$$

Changing variables to $y = kR_s \propto k(M/M_*)^{(5+n)/6}$, we see that

$$\Delta(k) \propto k^\gamma, \quad \gamma = \left(\frac{9+3n}{5+n} \right) - \alpha \left(\frac{3+n}{5+n} \right), \quad (32)$$

where the first term in γ is the prediction of stable clustering. The departure arises from the factor ν^α in the mass function, and would vanish only if $\alpha = 0$ or $n = -3$. This is the origin of the difference in $\Delta(k)$ at high k between the model prediction (solid curves) and the fitting formula (dotted curves) shown in Figures 3 and 4.

For the three-point function, the one-halo integral B_{1h}^{eq} in equation (29) converges (barely, for $p = \frac{3}{2}$ and $n = -2$), giving

$$\begin{aligned} B^{\text{eq}}(k) &\propto k^{\gamma_3-6}, & \gamma_3 &= 2 \left(\frac{9+3n}{5+n} \right) - \alpha \left(\frac{3+n}{5+n} \right) \\ Q^{\text{eq}}(k) &\propto k^{\alpha(3+n)/(5+n)} \end{aligned} \quad (33)$$

This again disagrees with the prediction of stable clustering that Q is constant, but it appears to be consistent with numerical simulations as shown in Figures 3 and 4.

For yet higher order correlations, details of the halo profile begin to matter. For $p = 1$, the pattern of equations (32) and (33) persists to all orders, but for $p = \frac{3}{2}$ they apply only for the two- and three-point functions; for four-point and higher functions the nonlinear scale M_* and $\gamma_n = np - 3$ for $n \geq 4$. Thus there seems to be some potentially interesting behavior that is tested only in the four-point function and higher.

7. Summary

We have presented an analytic model for the two- and three-point correlation functions $\xi(r)$ and $\zeta(r_1, r_2, r_3)$ of the cosmological mass density field and their Fourier transforms, the mass power spectrum $P(k)$ and the bispectrum $B(k_1, k_2, k_3)$. In this model, the clustering statistics of the density field are derived from a superposition of dark matter halos with a given set of input halo properties. These input ingredients include realistic halo density profiles of equation (2), halo mass distribution of equation (6), and halo-halo spatial correlations of equations (10) and (15). The main results of the model are given by equations (18) and (21) for the two-point statistics ξ and P , and by equations (25) and (29) for the three-point statistics ζ and B . This model provides a rapid way to compute the correlation functions over all length scales where the model inputs are valid; it also gives a physical interpretation of the clustering process of matter in the universe.

We have tested the validity of this model by comparing its predictions with results from cosmological simulations of an $n = -2$ scale-free model and a Λ CDM model. As Figures 3 – 6 illustrate, the model describes well the simulation results spanning the entire range of behavior from the perturbative regime on large scales to the strongly nonlinear regime on small scales. To probe the critical high- k range in the deeply nonlinear regime, we have used a halo replacement technique to increase the resolution of the large parent simulations. As Figures 1 and 2 illustrate, this method of replacing the original halos that suffer from numerically softened cores with synthetic halos of analytic profiles is a reasonable way to improve the resolution of numerical simulations. By using density profiles obtained empirically from higher-resolution simulations of individual halos, this recipe allows us to model accurately the inner regions of the halos on scales below the numerical softening length scale, while at the same time preserving all the large-scale information available in the large parent simulation. This technique should also be useful for other studies that depend on the inner halo density profiles, for example, the ray-tracing method in gravitational lensing.

Given that dark matter halos in simulations (and presumably in nature) are not perfectly spherical, cleanly delineated objects, it is intriguing that the model constructed in this paper works as well as it does at matching the simulation results. Nevertheless, this analytic model provides a good qualitative and quantitative description over the entire range of scales covered by the simulation, and it can be used to make predictions beyond these scales. This is the first model prescription that successfully reproduces both two- and three-point mass correlations. We believe that it will prove to be a generally useful framework.

We have enjoyed stimulating discussions with John Peacock and David Weinberg. We thank Edmund Bertschinger for valuable comments and for providing the $n = -2$ scale-free simulation. Computing time for this work is provided by the National Scalable Cluster Project and the Intel Eniac2000 Project at the University of Pennsylvania. C.-P. M. acknowledges support of an Alfred P. Sloan Foundation Fellowship, a Cottrell Scholars Award from the Research Corporation, a Penn Research Foundation Award, and NSF grant AST 9973461.

A. Appendix

In this Appendix we display analytic forms for the convolution of the dimensionless profile shape

$$\lambda(x) = \int d^3y u(y) u(|\mathbf{x} + \mathbf{y}|) \quad (\text{A1})$$

discussed in §3. These analytic expressions are useful for computing the nonlinear two-point correlation function ξ of the mass density field, which is dominated by the 1-halo term ξ_{1h} in equation (18) and is related to λ by

$$\xi(r) \approx \xi_{1h}(r) = \int dM \frac{dn}{dM} \bar{\delta}^2 R_s^3 \lambda(r/R_s), \quad \text{for } \xi \gtrsim 1. \quad (\text{A2})$$

For the type-I profile u_I of equation (2), the angular integration in equation (A1) is analytic, and λ is reduced to a simple integral

$$\lambda_I(x) = \frac{2\pi}{(2-p)x} \int_0^\infty \frac{y dy}{y^p (1+y)^{3-p}} \left[\frac{(x+y)^{2-p}}{(1+x+y)^{2-p}} - \frac{|x-y|^{2-p}}{(1+|x-y|)^{2-p}} \right]. \quad (\text{A3})$$

For the special case $p = 1$, this integral can be further reduced to the analytical form

$$\lambda_I(x) = \frac{8\pi}{x^2(x+2)} \left[\frac{(x^2 + 2x + 2) \ln(1+x)}{x(x+2)} - 1 \right], \quad p = 1. \quad (\text{A4})$$

For u_{II} of equation (2), we are able to simplify λ to

$$\lambda_{II}(x) = \frac{2\pi}{x} \int_0^\infty \frac{y dy}{y^p(1+y^{3-p})} F_p(x, y), \quad (\text{A5})$$

where the function $F_p(x, y)$ represents the angular part of the integration in equation (A1) and

$$F_p(x, y) = \int_{|x-y|}^{x+y} \frac{z dz}{z^p(1+z^{3-p})}. \quad (\text{A6})$$

The integral in F_p can be reduced to analytic forms for special values of p . Here we display the six cases $p = 0, 1/2, 1, 3/2, 2,$ and $5/2$:

$$\begin{aligned} F_0 &= \frac{1}{6} \left\{ 2\sqrt{3} \tan^{-1} \left[\frac{-1 + 2(x+y)}{\sqrt{3}} \right] + \ln \left[\frac{1 - (x+y) + (x+y)^2}{1 + 2(x+y) + (x+y)^2} \right] \right\} \\ &\quad - \frac{1}{6} \{ \text{replace } (x+y) \text{ above with } |x-y| \} \\ F_{1/2} &= \frac{1}{10} \left\{ -2\sqrt{10 + 2\sqrt{5}} \tan^{-1} \left(\frac{1 + \sqrt{5} - 4\sqrt{x+y}}{\sqrt{10 - 2\sqrt{5}}} \right) \right. \\ &\quad \left. - 2\sqrt{10 - 2\sqrt{5}} \tan^{-1} \left(\frac{-1 + \sqrt{5} + 4\sqrt{x+y}}{\sqrt{10 + 2\sqrt{5}}} \right) \right\} \end{aligned} \quad (\text{A7})$$

$$\begin{aligned}
 & +4 \ln (1 + \sqrt{x+y}) - (1 + \sqrt{5}) \ln \left[1 + \frac{1}{2}(-1 + \sqrt{5})\sqrt{x+y} + x + y \right] \\
 & - (1 - \sqrt{5}) \ln \left[1 - \frac{1}{2}(1 + \sqrt{5})\sqrt{x+y} + x + y \right] \Big\} \\
 & - \frac{1}{10} \{ \text{replace } (x+y) \text{ above with } |x-y| \}
 \end{aligned} \tag{A8}$$

$$F_1 = \tan^{-1}(x+y) - \tan^{-1}(|x-y|) \tag{A9}$$

$$\begin{aligned}
 F_{3/2} &= \frac{1}{3} \left\{ 2\sqrt{3} \tan^{-1} \left[\frac{-1 + 2\sqrt{x+y}}{\sqrt{3}} \right] + \ln \left[\frac{1 + 2\sqrt{x+y} + x + y}{1 - \sqrt{x+y} + x + y} \right] \right\} \\
 & - \frac{1}{3} \{ \text{replace } (x+y) \text{ above with } |x-y| \}
 \end{aligned} \tag{A10}$$

$$F_2 = \ln \left[\frac{x+y}{1+x+y} \right] - \ln \left[\frac{|x-y|}{1+|x-y|} \right] \tag{A11}$$

$$F_{5/2} = \frac{2}{\sqrt{|x-y|}} - \frac{2}{\sqrt{x+y}} + \ln \left[\frac{(1 + 2\sqrt{x+y} + x + y) |x-y|}{(1 + 2\sqrt{|x-y|} + |x-y|)(x+y)} \right] \tag{A12}$$

REFERENCES

- Cole, S., & Lacey, C. 1996, MNRAS, 281, 716
- Davis, M., & Peebles, P. J. E. 1977, ApJS, 34, 425
- Dubinski, J., & Carlberg, R. 1991, ApJ, 378, 496
- Ferrell, R., & Bertschinger, E. 1994, Int. J. Mod. Phys. C, 5, 933
- Fry, J. N., 1984, ApJ, 279, 499
- Fry, J. N., & Peebles, P. J. E. 1978, ApJ, 221, 19
- Fukushige, T., & Makino, J. 1997, ApJ, 477, L9
- Groth, E. J., & Peebles, P. J. E. 1977, ApJ, 217, 385
- Hamilton, A. J. S., Matthews, A., Kumar, P., & Lu, E. 1991, ApJ, 374, L1
- Hernquist, L. 1990, ApJ, 356, 359
- Huss, A., Jain, B., & Steinmetz, M. 1999, ApJ, 517, 64
- Jain, B., & Bertschinger, E. 1998, ApJ, 509, 517
- Jain, B., Mo, H. J., & White, S. D. M. 1995, MNRAS, 276, L25
- Jenkins, A., Frenk, C. S., White, S. D. M., Colberg, J. M., Cole, S., Evrard, A. E., & Yoshida, N. 2000, astro-ph/0005260
- Jing, Y. P. 1998, ApJ, 503, L9
- Jing, Y. P., & Suto, Y. 2000, ApJ, 529, L69
- Kravtsov, A. V., & Klypin, A. 1999, ApJ, 520, 437
- Ma, C.-P. 1998, ApJ, 508, L5
- Ma, C.-P., Caldwell, R. R., Bode, P., & Wang, L. 1999, ApJ, 521, L1
- Ma, C.-P., & Fry, J. N. 2000a, ApJ, 531, L87
- Ma, C.-P., & Fry, J. N. 2000c, ApJ, in press (astro-ph/0005233)
- McClelland, J., & Silk, J. 1977, ApJ, 217, 331
- Mo, H. J., & White, S. D. M. 1996, MNRAS, 282, 347
- Mo, H. J., Jing, Y. P., & White, S. D. M. 1997, MNRAS, 284, 189

- Moore, B., Governato, F., Quinn, T., Stadel, J., & Lake, G. 1998, *ApJ*, 499, L5
- Moore, B., Quinn, T., Governato, F., Stadel, J., & Lake, G. 1999, *MNRAS*, 310, 1147
- Navarro, J. F., Frenk, C. S., & White, S. D. M. 1996, *ApJ*, 462, 563
- Navarro, J. F., Frenk, C. S., & White, S. D. M. 1997, *ApJ*, 490, 493
- Neyman, J., & Scott, E. L. 1952, *ApJ*, 116, 144
- Peacock, J. A., & Dodds, S. J. 1996, *MNRAS*, 280, L1
- Peebles, P. J. E. 1974, *A&A*, 32, 197
- Peebles, P. J. E. 1980, *The Large-Scale Structure of the Universe* (Princeton: Princeton Univ. Press)
- Peebles, P. J. E., & Groth, E. J. 1975, *ApJ*, 196, 1
- Press, W. H., & Schechter, P. 1974, *ApJ*, 187, 425
- Scherrer, R. J., & Bertschinger, E. 1991, *ApJ*, 381, 349
- Seljak, U. 2000, *astro-ph/0001493*
- Sheth, R. K., & Jain, B. 1997, *MNRAS*, 285, 231
- Sheth, R. K., & Tormen, G. 1999, *MNRAS*, 308, 119
- Tormen, G., Bouchet, F., & White, S. D. M., 1997, *MNRAS*, 286, 865
- Valageas, P. 1998, *A&A*, 347, 757
- Yano, T., & Gouda, N. 1999, *astro-ph/9906375*

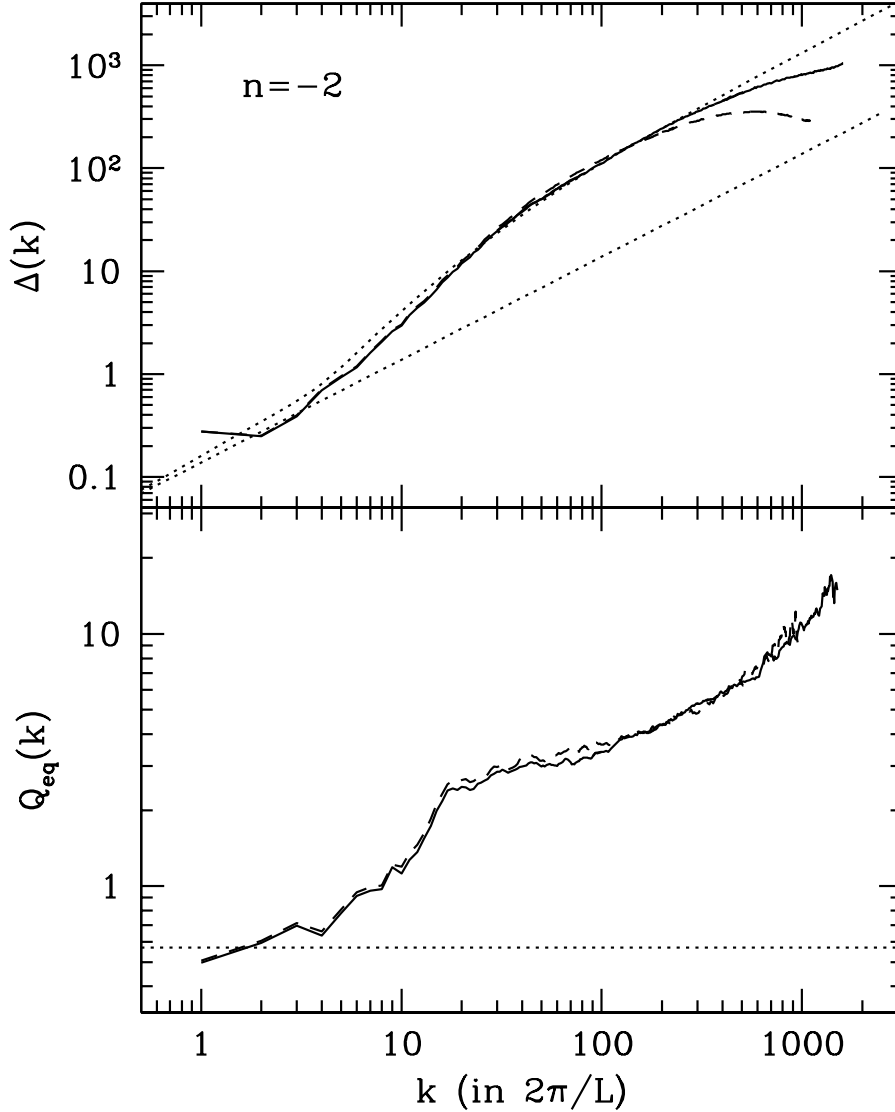


Fig. 1.— Effects on the power spectrum (upper panel) and bispectrum (lower panel) when the dark matter halos in an $n = -2$ scale-free simulation are replaced with synthetic halos of density profile $u_{II}(x) = 1/(x^{3/2} + x^3)$ and concentration parameter $c(M) = 3(M_*/M)^{1/6}$ (see §2 for definitions). The dashed and solid curves are for the original and the redistributed particles, respectively. They agree up to $k \approx 200$ (in $2\pi/L$), beyond which the dashed curves deviate due to the finite resolution in the original simulation. The dotted curves show the linear Δ and the nonlinear fitting of Jain et al. (1995) in the upper panel, and the lowest-order perturbative result $Q^{(0)} = 4/7$ in the bottom panel.

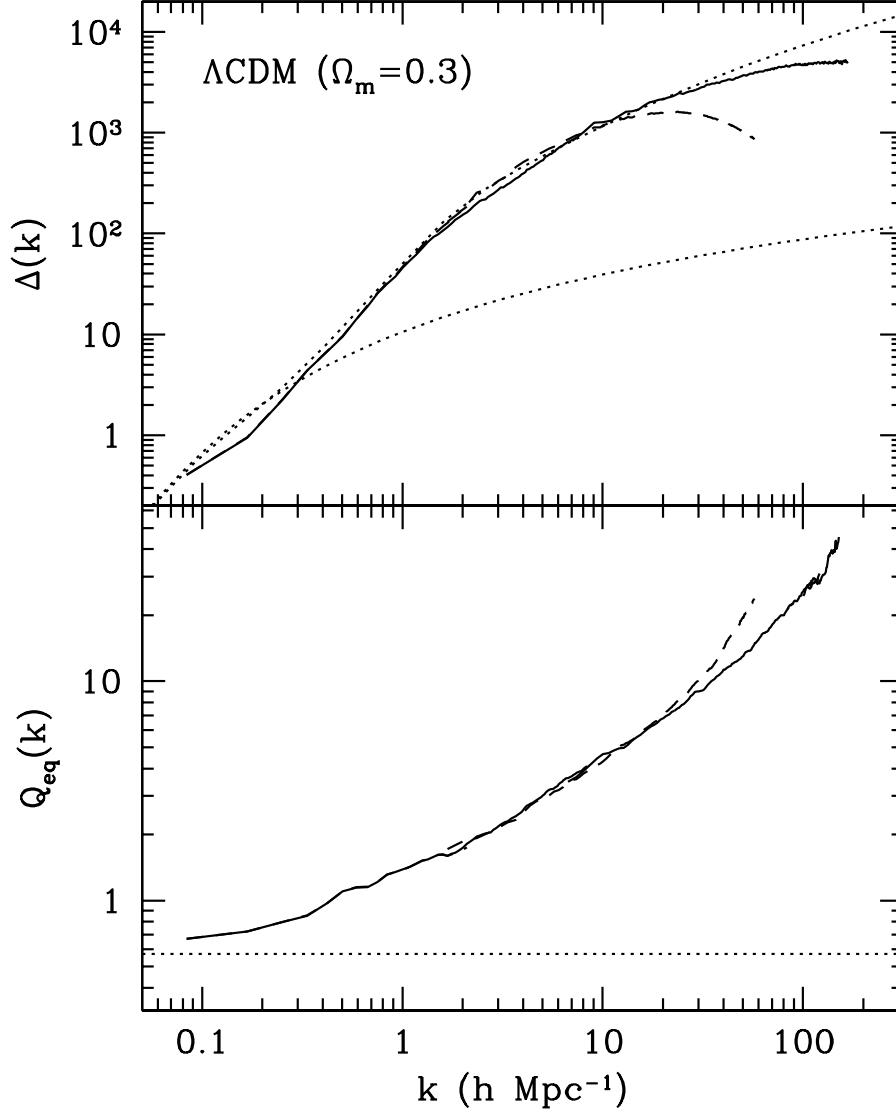


Fig. 2.— Same as Fig. 1 but for a low-density CDM simulation with $\Omega_m = 0.3, \Omega_\Lambda = 0.7$. The synthetic halos have the $u_{II}(x) = 1/(x^{3/2} + x^3)$ profile and concentration parameter $c(M) = 5(M^*/M)^{1/6}$. Again, the original (dashed) and redistributed (solid) particles have similar $\Delta(k)$ and $Q_{\text{eq}}(k)$ up to the simulation resolution of $k \approx 20 h \text{ Mpc}^{-1}$.

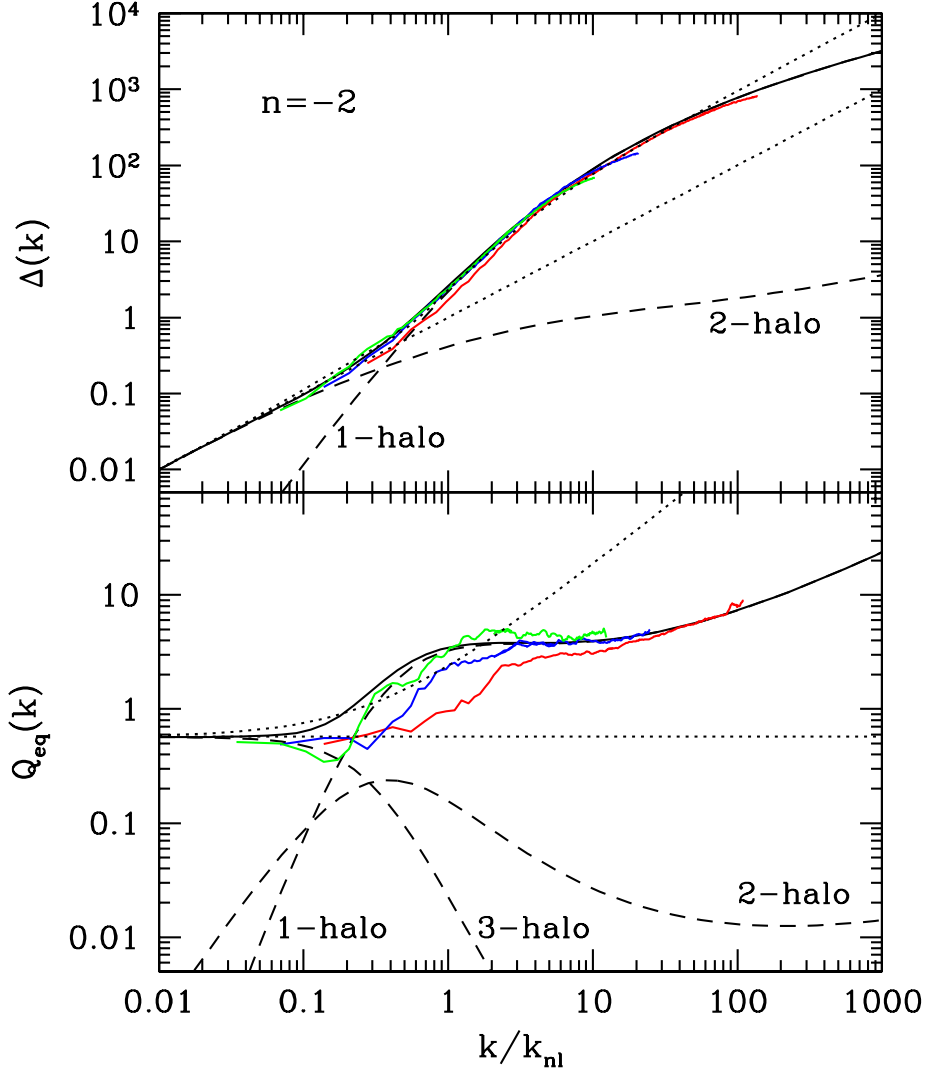


Fig. 3.— N -body results vs. predictions of the analytic model of §2–§4 for the power spectrum (upper) and bispectrum (lower) for the $n = -2$ scale-free model. The dashed curves show the separate contributions to Δ and Q_{eq} computed from the single- and multiple-halo terms of eqs. (21) and (29); the solid black curves show the sum predicted by the model. The colored curves show the N -body results, where synthetic halos have been used to extend the curves to higher k . (The same density profile and $c(M)$ are used for the synthetic halos and the analytic model.) Three simulation outputs are shown, where the expansion factor (1 initially) and nonlinear wavenumber (in units of $2\pi/L$) are: $(a, k_{\text{nl}}) = (13.45, 29)$, $(19.03, 14.5)$, and $(26.91, 7.25)$ (from left to right in green, blue and red). Three of the four dotted curves are the same as in Fig. 1; the rising one in the bottom panel shows the 1-loop Q .

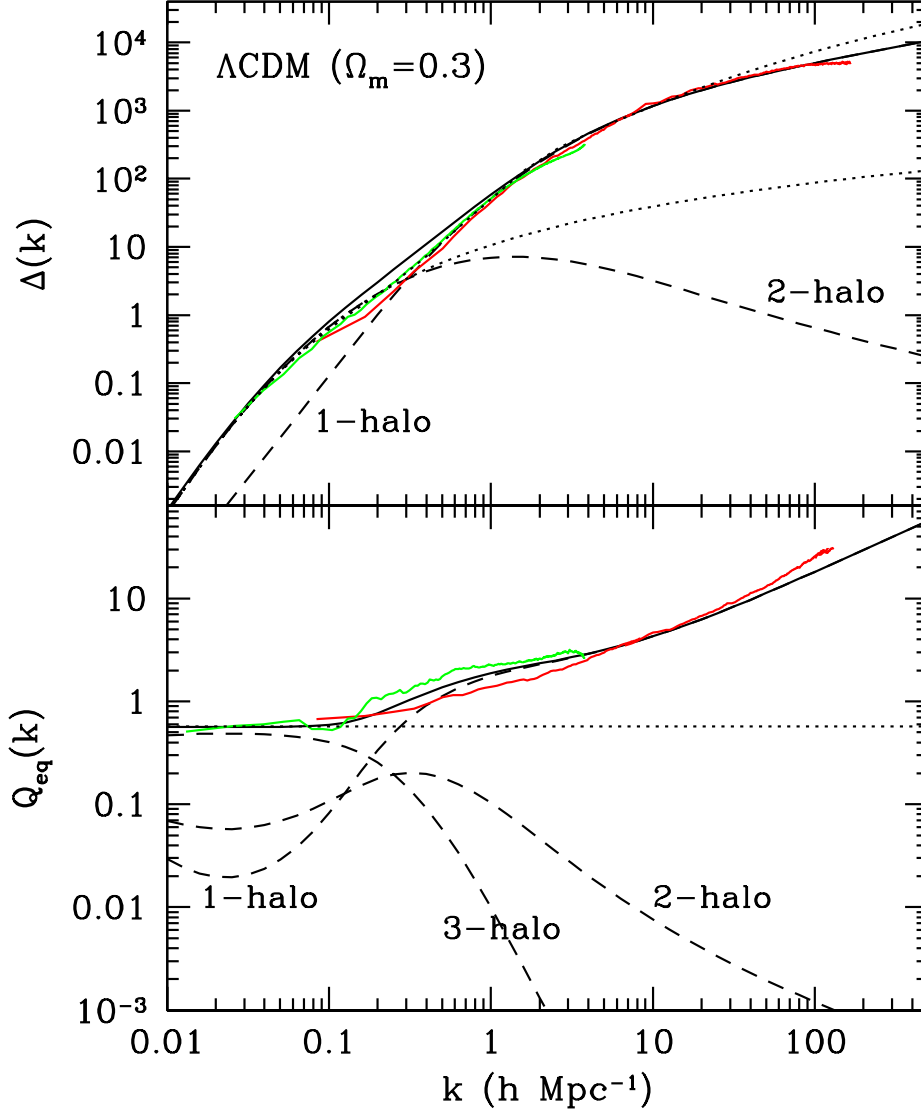


Fig. 4.— Same as Fig. 3 but for the low-density CDM simulation with $\Omega_m = 0.3, \Omega_\Lambda = 0.7$. The red and green curves are computed from a $(100 \text{ Mpc})^3$ and a $(640 \text{ Mpc})^3$ simulation, respectively.

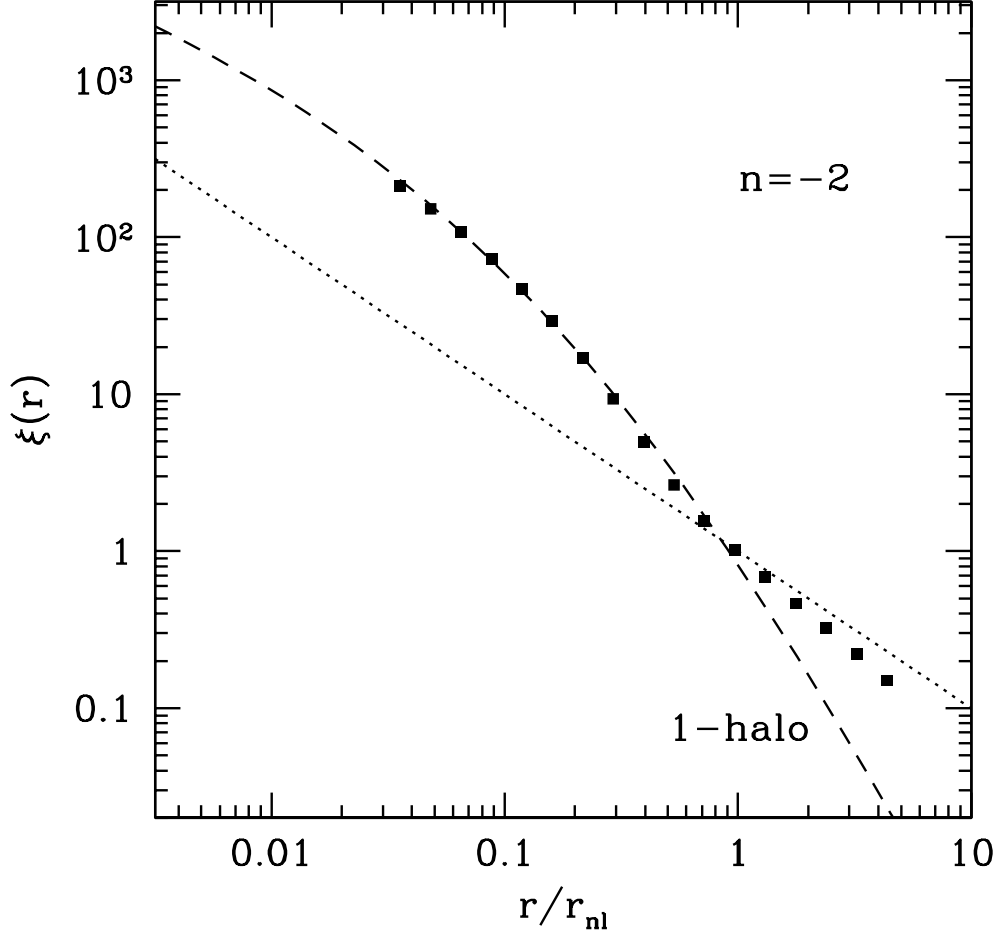


Fig. 5.— N -body results vs. predictions of the analytic model of §2–4 for the two-point correlation function $\xi(r)$ for the $n = -2$ model. The dashed curve shows the 1-halo term $\xi_{1h}(r)$ of equation (18) from our analytic model. The solid squares show $\xi(r)$ computed directly from an N -body simulation. The two agree very well for $r/r_{nl} \lesssim 1$. The dotted curve shows the linear theory $\xi_{lin}(r) = r_{nl}/r$.

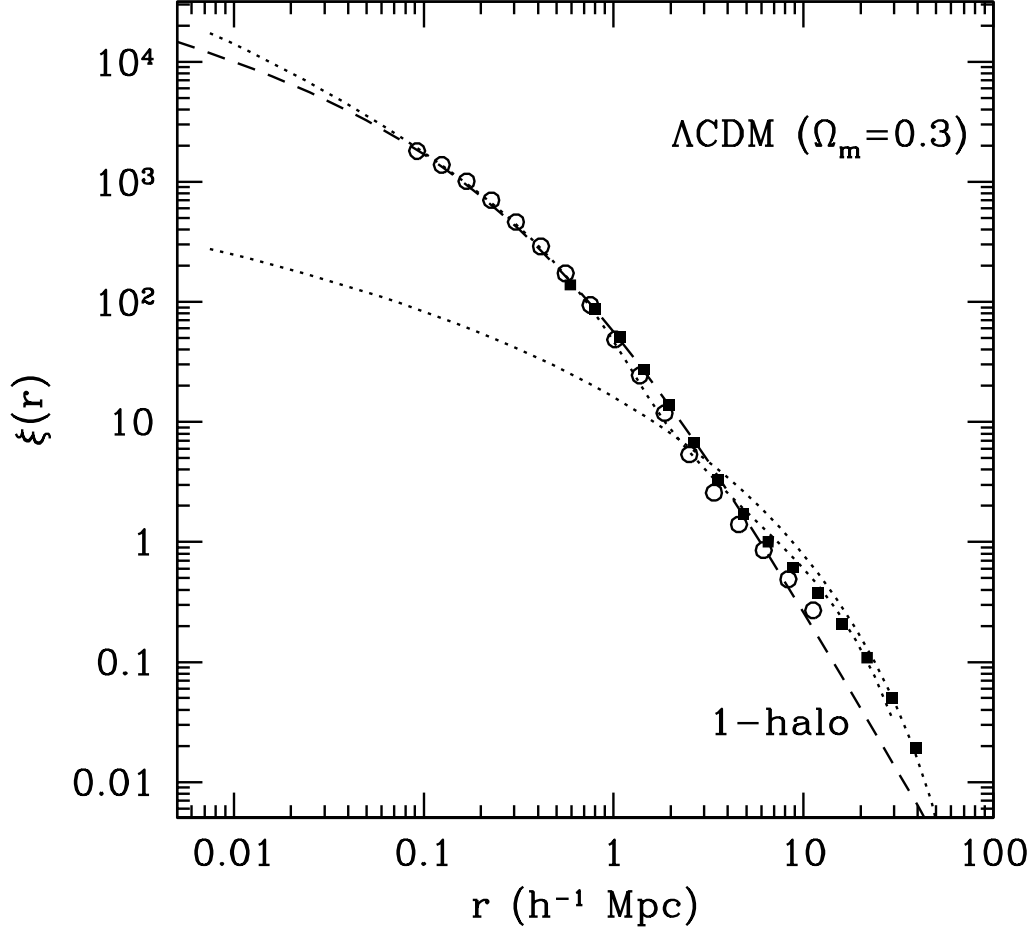


Fig. 6.— Same as Fig. 5 but for the Λ CDM model. The symbols show $\xi(r)$ computed from a $(100 \text{ Mpc})^3$ (open circles) and a $(640 \text{ Mpc})^3$ (solid squares) N -body simulation. The dotted curves show $\xi_{\text{lin}}(r)$ from the linear theory (lower curve) and the nonlinear $\xi(r)$ (upper curve) given by the fitting formula of Ma (1998).